Field Reconnaissance after the 25 April 2015 M 7.8 Gorkha Earthquake

by Stephen Angster, Eric J. Fielding, Steven Wesnousky, Ian Pierce, Deepak Chamlagain, Dipendra Gautam, Bishal Nath Upreti, Yasuhiro Kumahara, and Takashi Nakata

ABSTRACT

Fault scarps and uplifted terraces in young alluvium are frequent occurrences along the trace of the northerly dipping Himalayan frontal thrust (HFT). Generally, it was expected that the 25 April 2015 **M** 7.8 Gorkha earthquake of Nepal would produce fresh scarps along the fault trace. Contrary to expectation, Interferometric Synthetic Aperture Radar and aftershock studies soon indicated the rupture of the HFT was confined to the subsurface, terminating on the order of 50 km north of the trace of the HFT. We undertook a field survey along the trace of the HFT and along faults and lineaments within the Kathmandu Valley eight days after the earthquake. Our field survey confirmed the lack of surface rupture along the HFT and the mapped faults and lineaments in Kathmandu Valley. The only significant ground deformation we observed was limited to an ~1–km-long northeast-trending fracture set in the district of Kausaltar within Kathmandu. This feature is interpreted not to be the result of tectonic displacement, but rather a localized extension along a ridge. Our survey also shows the ubiquitous presence of fallen chimneys of brick kilns along the HFT and within the Kathmandu Valley. Measurements of a small subset of fallen chimneys across the region suggest a degree of systematic fall direction of the chimneys when subdivided geographically.

Online Material: Color versions of Figures 3 and 4; additional photographs of the Kausaltar fracture.

INTRODUCTION

Shortly after the 25 April 2015 **M** 7.8 Gorkha, Nepal, earthquake (Fig. 1), it became apparent that the event was a result of thrusting along the main Himalayan thrust (Northern California Earthquake Data Center [NCEDC], 2015; see Data and Resources). Continental earthquakes of this size generally produce surface rupture (Wesnousky, 2008). This fact served as the initial motivation to mount a field reconnaissance of the area soon after the event. Our reconnaissance was an international collaboration guided by Interferometric Synthetic Aperture Radar (InSAR) maps developed in the weeks after the event (e.g., Lindsey *et al.*, 2015; Advanced Rapid Imaging and Analysis (ARIA) Center and the Geospatial Authority of Japan [see Data and Resources]) and prior mapping of fault and lineament traces along the active surface expression of the Himalayan frontal thrust (HFT) (Nakata, 1989; Nakata *et al.*, 1984; Bollinger *et al.*, 2014) and in the Kathmandu Valley (e.g., Asahi, 2003). Here, we report our findings arising from our visit to the area between 4 and 15 May 2015.

INSAR

InSAR interferograms of the epicentral region were constructed soon after the event and quickly posted to the Internet (e.g., Lindsey *et al.*, 2015; ARIA Center and Geospatial Authority of Japan [see Data and Resources]). Figure 1 shows the interferogram from a Japanese Aerospace Exploration Agency (JAXA) Advanced Land Observation Satellite-2 (ALOS-2) wide-swath (ScanSAR) interferogram on descending (west-looking) path 48, with data acquired on 21 February and 2 May 2015 and processed by the Caltech-Jet Propulsion Laboratory ARIA project (see Data and Resources). InSAR analysis was done with a modified version of the InSAR Scientific Computing Environment software (Rosen *et al.*, 2012 and Liang and Fielding, unpublished manuscript, 2015). The Global Positioning System (GPS) offset vectors in Figure 1 were also processed by the ARIA project (see Data and Resources).

The interferogram of the region (shown in Fig. 2) was constructed from ALOS-2 ascending path 157 (east-looking) satellite passes on 21 February 2015 and 2 May 2015, bracketing the time of the mainshock. This interferogram is from ALOS-2 strip map beam SM3; it was processed with 8 × 16 looks (pixels averaged) in the range (across-track) and azimuth (along-track) directions (radar image postings of 80 m) and geocoded at a final pixel spacing of 30 m. Features down to ~100 m horizontal scale should be detectable. Each color fringe of Figure 2 depicts 10 cm of ground displacement in the radar line-of-sight direction, which varies from 34° to 39° from the vertical across the fine-beam swath. The wavelength of the ALOS-2 radar is 24 cm, so the original radar fringes indicate relative surface displacements of 12 cm per fringe. Surface displacements in these images

 doi: 10.1785/0220150135

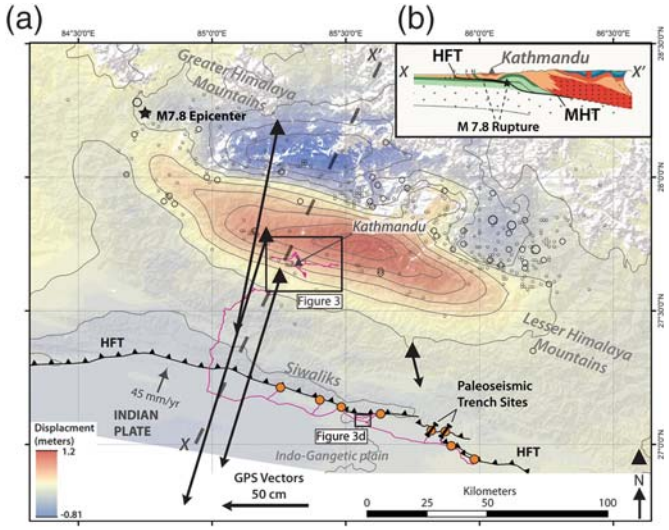

▲ **Figure 1.** (a) Overview map of Gorkha earthquake rupture region. The red (up) and blue (down) colors display line-of-sight motion measured from Advanced Land Observation Satellite 2 (ALOS-2) wide-swath Interferometric Synthetic Aperture Radar (InSAR) data, almost all due to vertical displacements. Contours are 20 cm of the InSAR motion. Global Positioning System (GPS) stations (black triangles) show horizontal motion. Aftershock distribution outlines approximate the extent of the fault rupture. Relative sizes of aftershocks (**M** <4) are shown by open circles (National Seismological Centre of Nepal [NSCN], 2015; see Data and Resources). The pink lines show tracks of our reconnaissance work. The orange circles represent sites visited along the Himalayan frontal thrust (HFT). Paleoseismic trench sites of Lave *et al.* (2005) and Sapkota *et al.* (2013) are indicated on the map along the HFT. (b) The inset shows a general cross section across the plate boundary and approximate extent of the Gorkha earthquake rupture along the main Himalayan thrust (MHT). The generalized rupture area is indicated by the thick black line. The HFT is the active surface expression of the MHT.

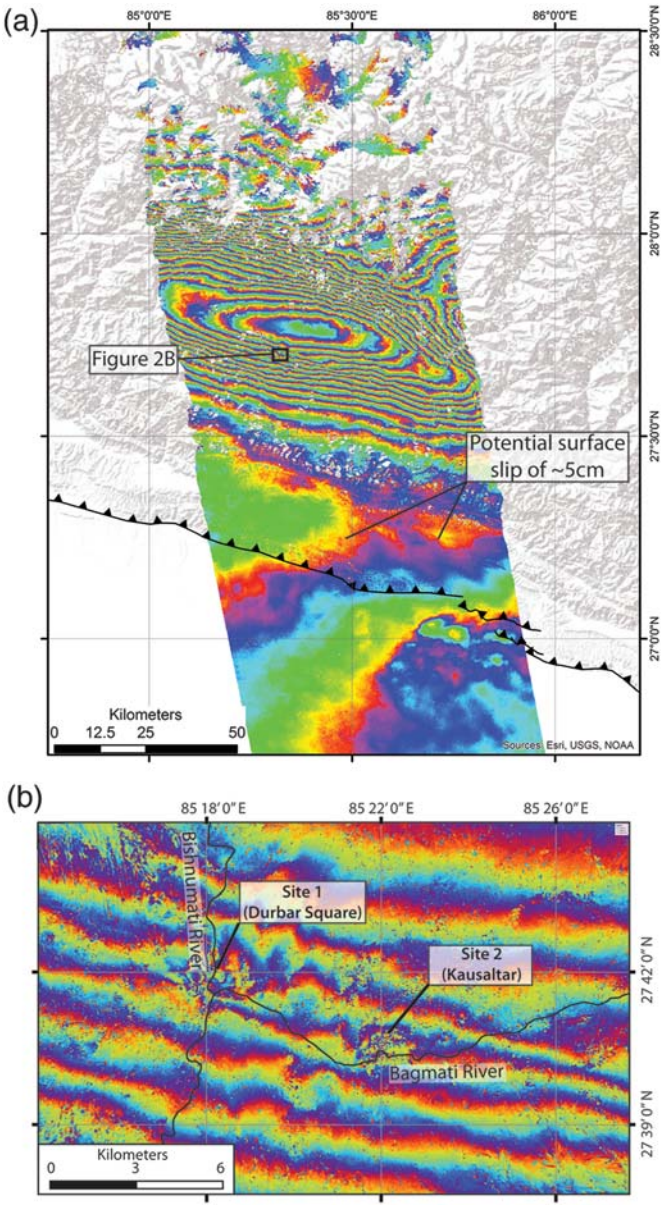

▲ **Figure 2.** (a) InSAR interferogram of the rupture region constructed from ALOS-2 fine-beam passes on 21 February 2015 and 2 May 2015. Each color fringe depicts 10 cm of displacement (slightly different from original ALOS-2 fringes). (b) Enlarged area of the fine-beam interferogram in Kathmandu showing the disturbance of fringes (each equivalent to 10 cm) that is consistent with a north-trending zone of ground deformation at site 1 and east-trending zone at site 2. The thin black lines show the trace of the Bagmati and Bishnumati rivers.

are generally represented by discontinuities in the contours. There are no major discontinuities at the scale of Figure 2a. This interferogram, and those made by others, soon led to the interpretation that the earthquake rupture was confined to the subsurface (e.g., Berberian, 1995; Yeats and Lillie, 1991).

Discontinuities of about 1/8 of a fringe (or around 1.5 cm for ALOS-2) should be visible where the interferogram is coherent, which is true everywhere except in the snow-covered highest peaks of the Himalayas and a few areas of intense agriculture. In addition, if the main rupture slip approached the surface, it would have caused deflection of the fringes and steeper fringe gradients. There are no large-scale fringes anywhere near the HFT, which rules out any significant slip on that fault. Atmospheric effects that are the largest source of uncertainty in the interferogram measurements have larger spatial scales and would not hide discontinuities due to surface ruptures. There is only one area of likely triggered shallow slip on a fault immediately north of the HFT between 27.242° N, 85.510° E and 27.241° N, 85.693° E (Fig. 2a). At that location, there is up to ~5 cm of slip at the surface in the radar line-of-sight but only on the very shallow part of the fault (less than ~500 m depth). This feature was also observed on a Sentinel-1 coseismic interferogram (Fielding, *et al.*, in preparation) and confirmed with field observation in Martin *et al.* (2015).

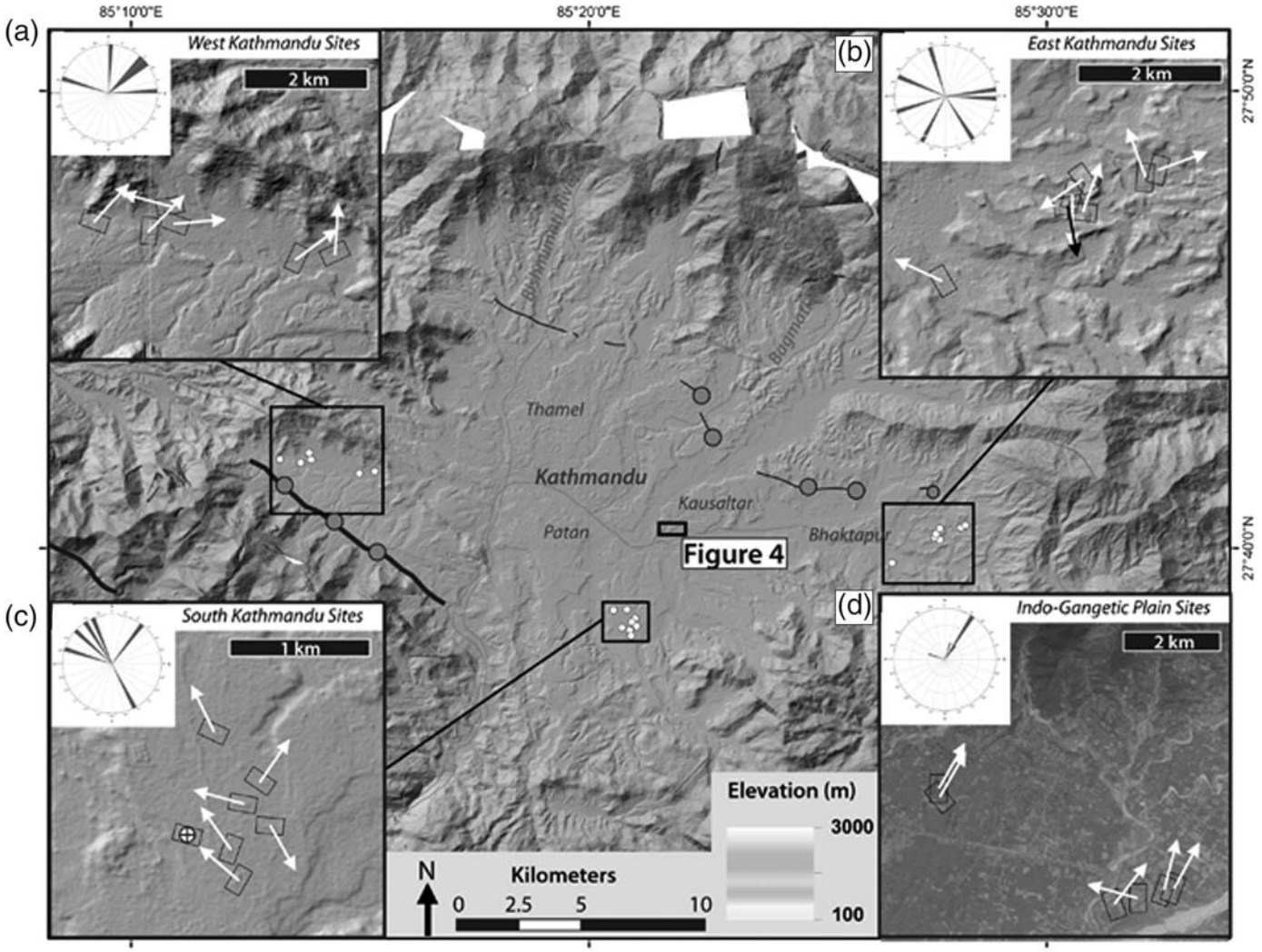

▲ **Figure 3.** Hillshade image of Kathmandu Valley developed from an 8 m digital elevation model (Noh *et al.*, 2015). The solid dots indicate sites traversed locally and queried local inhabitants. Thick black lines indicate previously mapped faults and thin black lines indicate newly defined lineaments. The inset corner figures are enlarged views of indicated areas displaying chimney data collected at the (a) east, (b) west, and (c) south Kathmandu Sites. (d) Chimney data from the Indo-Gangetic Plain are shown (see Fig. 1 for location). White arrows show fall direction from mainshock and black arrow shows fall direction resulting from large aftershock. Ⓔ A color version of this figure is available in the electronic supplement as Figure S1.

Figures 1 and 3 show the sites visited along the HFT, previously mapped faults in southern Kathmandu Valley (Asahi, 2003), and suspected scarp features in the northern part of the valley (see Fig. 3). Our checks at each fault or lineament crossing included traverses along the faults and interviews of local inhabitants. At no locations did we observe or hear of ground ruptures along the respective fault lines.

The InSAR within Kathmandu Valley revealed minor interruption of interferogram fringes at two sites (Fig. 2b). The sites are labeled 1 and 2 in Figure 2b and located in the vicinity of Durbar Square and the community of Kausaltar. The disruption of fringes at site 1 trend approximately north–south and just to the east of the north-trending Bishnumati River, a tributary of the larger Bagmati. Our traverses through the area and queries with locals in the densely populated area uncovered no lineaments of significant damage or ground disturbance. In contrast, however, ground disturbance and building damage were observed to clearly correlate to the disruptions of fringes in the area of site 2 in Kausaltar and are described in the following section.

KAUSALTAR FRACTURES

The disruptions in the interferogram fringes at site 2 (Fig. 2b) led us to a newly developed set of fractures that opened during the main earthquake, which caused significant damage to building structures and roads, ~1.5 km south-southeast of the Kathmandu International Airport (Fig. 3). We used large-scale Google Earth imagery and hand-held GPS units to locate and map the newly developed fractures in Kausaltar (Fig. 4). We also

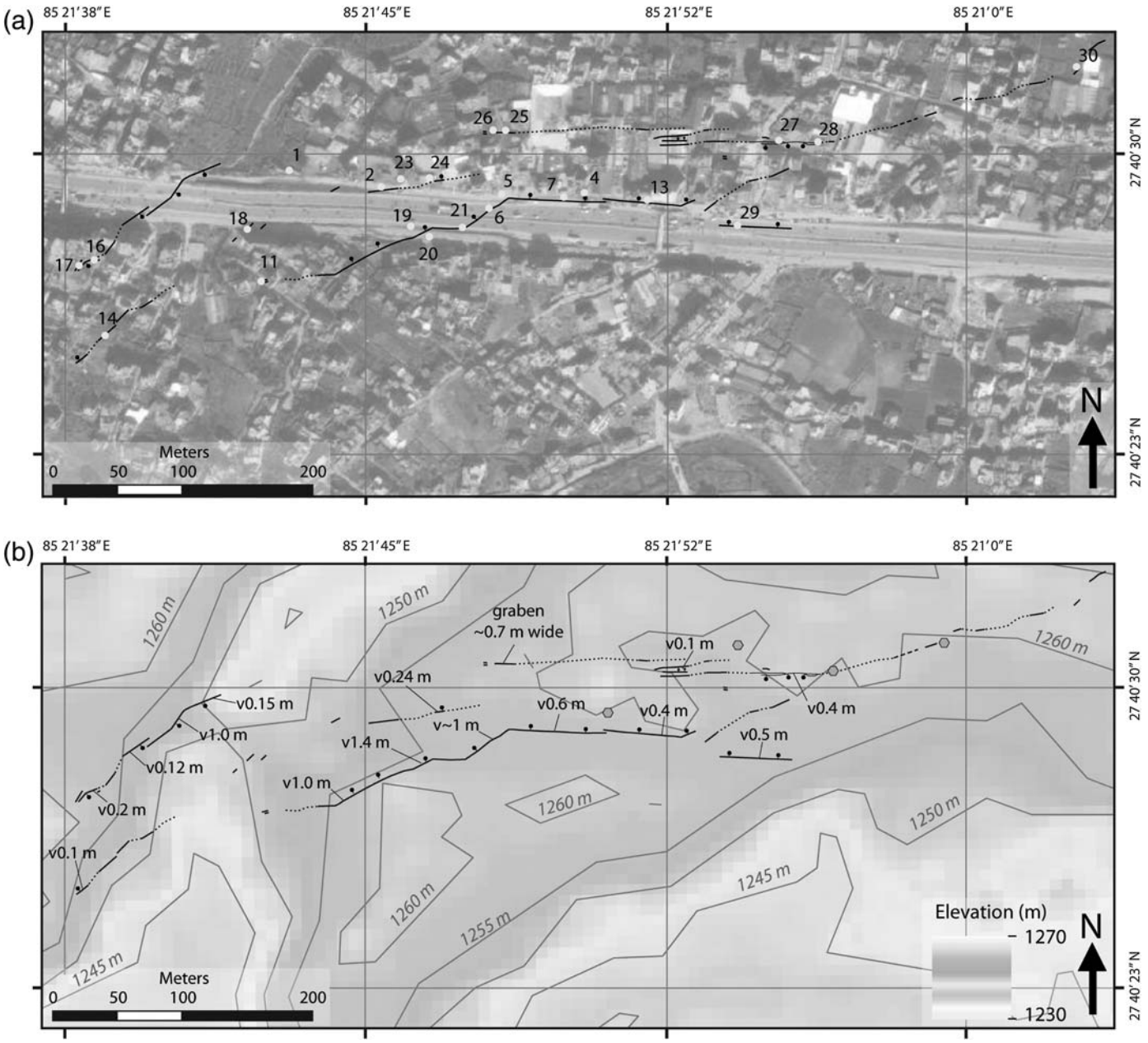

▲ **Figure 4.** (a) Locations of the northeast-trending Kausaltar fracture set. Black barbells show the downthrown side of each fracture. The solid dots show locations of associated photos in the Ⓔ electronic supplement. (b) Same-scale map of fractures and field measurements underlain by the hillshade image (Noh *et al.*, 2015). Contours are at 5 m intervals. Ⓔ A color version of this figure is available in the electronic supplement as Figure S2.

collected vertical and horizontal offset measurements (Fig. 4b). In addition to the fractures, we mapped the location of four deep (~45 m) water wells within the mapped area (Fig. 4b).

The mapped fractures extend along a northeast trend for ~730 m, cutting across roads, small open fields, and building structures (Fig. 4a). A local resident observed some of these fractures opening ~30 s after the strong shaking from the mainshock (R. Bilham, personal comm., 2015). The fractures displayed 0.1–1.5 m vertical scarps facing both north-northwest and south-southeast, indicated with black barbells on the down-dropped side in Figure 4a,b. Horizontal extensions across the fractures ranged from 0 to 20 cm. Minimal lateral strike-slip motion of < 15 cm in both directions was observed and measured on several fractures.

A topographic analysis using an 8 m digital elevation model developed from DigitalGlobe imagery (Noh *et al.*, 2015) shows that these fractures trend along a topographic high between two drainages (Fig. 4b). The four deep-water wells also trend along this topographic high, paralleling the fracture trend. The spatial association of the wells and fracture set is intriguing; however, structural mapping of the area and the well histories is needed to confirm a causal association but is unavailable.

▲ **Figure 5.** Example photographs of the newly developed fracture set in Kausaltar. The number in the upper left corner gives the location number indexed to the map of shown in Figure 4a. Additional color photographs of Kausaltar fractures are provided in the Ⓔ electronic supplement.

Bidirectional-facing scarps and the varied amount of horizontal extension across these fractures suggest that these are the result of local extension. Our observations limit net extension across the deformation zone to <20 cm. Prior geophysical studies further indicate that there are no major basement structures underlying this portion of the Kathmandu Valley (Paudyal *et al.*, 2012). Together these observations suggest the zone of disturbance is not the result of deep-seated tectonic displacement, but rather cause by local site conditions and shaking.

Figure 5 illustrates the character of ground and building deformations. Locations of other photos along the trace taken soon after the event are indexed on the fault trace map of Figure 4a and are provided in the electronic supplement (Ⓔ Figs. S3–S27).

ADDITIONAL OBSERVATIONS—DAMAGED CHIMNEYS

Brick factories are abundant in Nepal, and it became apparent upon our geologic reconnaissance that most (but not all) of the

▲ **Figure 6.** Representative photo of a failed chimneystack located on the Indo-Gangetic Plain.

chimneystacks of the factories failed in a partial manner during the main earthquake. Failure of these chimneys generally resulted in toppling of the upper portion of the chimneys, leaving 10–30 m of the bottom part of the chimney remaining. A detailed engineering analysis of these failures is beyond the scope of this note, though the toppling characteristic appears in general accord with numerical analyses of chimney failures (e.g., Pallares *et al.*, 2011). The image of Figure 6 represents a common sight of a failed chimney.

The factories are set up on loam deposits in which bricks are excavated and cast onsite. The kilns are located onsite and laid out as 50–100 m long × 25–40 m wide rectangles, each with a single 30–40 m tall, upwardly tapering, cylindrical chimney that has 5–7 m basal diameter (Fig. 6). Construction of the generally unreinforced brick masonry chimneys is documented more thoroughly in Bonapace and Sestini (2003).

A survey of all the hundreds of brick kilns across the source region (see Ⓔ Fig. S28) of the Gorkha earthquake and HFT was also beyond the scope of our visit. However, we did examine the direction and manner in which the chimneys failed in the four separate areas shown in Figures 1 and 3. Three of the areas are within Kathmandu Valley (Fig. 3) and the other is on the Indo-Gangetic Plain, just south of the HFT (Fig. 1). Maximum intensities reported by Martin *et al.* (2015) generally range from European Macroseismic Scale (EMS) VII to VIII in Kathmandu Valley and EMS VI to VII along the HFT. The inset maps (a–d) of Figure 3 display the data collected at the four sites. The black rectangles represent the orientation of the kiln, and an arrow shows the chimney fall direction, summarized by rose plots in the upper left corners of each site (Fig. 3). We assume that the chimneys fell during the mainshock (white arrows), though in one case we were informed that failure occurred during the **M** 7.3 aftershock 16 days later (black arrow). White arrows show fall direction from mainshock and black arrow shows fall direction resulting from large aftershock.

The direction of chimney failure is not systematic when viewed across the four regions (Fig. 3). However, some consistency in fall directions is found when looking at each region individually. The azimuth of chimney falls at the west Kathmandu sites lie within the northeast quadrant in all but one case (Fig. 3a). Similarly, all but one of the chimney falls at south Kathmandu sites (Fig. 3c) near the southern edge of Kathmandu Valley align, in this case to the northwest. In contrast, chimney fall directions are essentially random in the area located at the east Kathmandu sites (Fig. 3b). The randomness of chimney falls in this region perhaps relates to its relatively more rugged topography as compared to the two prior regions. The remaining region is located just south of the HFT (Fig. 1) in the Indo-Gangetic Plain. Here, with one exception, the chimneys falls display a consistent northeasterly direction (Fig. 3d).

The sample size is small and arguably not definitive; however, it suggests that a more detailed study of the entire data set of the kiln chimneys in this and future earthquakes may reveal observations important to understanding characteristics of earthquake strong ground motion (e.g., Pallares *et al.*, 2006; Hinzen, 2009).

DISCUSSION AND CONCLUSION

Our brief field survey, in concert with development of InSAR interferograms by the authors and others, confirmed the Gorkha earthquake did not produce surface rupture along the HFT. The focal mechanism and aftershock distribution of the event (e.g., the U.S. Geological Survey National Earthquake Information Center; see Data and Resources) indicate the event was confined to the subsurface and stopped ∼50 km north of the trace of the HFT (Fig. 1). The presence of large scarps in young alluvium, geomorphic evidence of progressive offset of faulted terraces, and paleoseismic studies along the HFT to the south of the Gorkha earthquake suggest that there are indeed earthquakes that rupture the HFT (e.g., Nakata *et al.*, 1984; Nakata, 1989; Lave *et al.*, 2005; Sapkota *et al.*, 2013; Bollinger *et al.*, 2014). Yet, hazard assessments along this and other sections of the HFT now will be further complicated by uncertainty in how slip on the remaining southward 50 km section of the HFT will be accommodated. Will it take place by (1) postseismic creep along the now unruptured portion of the HFT, (2) a future earthquake limited to the shallowest southern section of the HFT, or (3) a larger earthquake that

slips along the entire decollement including that portion which ruptured in 2015? These questions will now certainly be at the center of discussion of past and future paleoseismic studies and hazard assessments along the HFT.

DATA AND RESOURCES

Advanced Land Observation Satellite 2 (ALOS-2) data and the Interferometric Synthetic Aperture Radar (InSAR) maps used for field guidance were obtained from Advanced Rapid Imaging and Analysis (ARIA) Center at http://aria.jpl.nasa.gov/node/43 (last accessed May 2015) and Geospatial Authority of Japan at http://www.gsi.go.jp/cais/topic150429-index-e.html (last accessed May 2015). Zipped keyhole markup language (KMZ) files for the interferograms in this paper are posted at the aria-share.jpl.nasa.gov website (http://aria-share.jpl.nasa.gov/events/20150425-Nepal_EQ/interferogram/, last accessed June 2015). The Global Positioning System offset vectors in Figure 1 were processed by Caltech-Jet Propulsion Laboratory's ARIA project and are available online (http://aria-share.jpl.nasa.gov/events/20150425-Nepal_EQ/GPS/20150425Nepal_ARIA_Final_Offsets_v4.txt, last accessed June 2015). The referenced focal mechanisms can be found at http://ncedc.org (last accessed May 2015) and http:earthquake.usgs.gov (last accessed May 2015). Liang and Fielding, unpublished manuscript, 2015, Interferometric Processing of ScanSAR Data Using Stripmap Processor: New Insights from Coregistration, IEEE Transactions on Geoscience and Remote Sensing. Google Earth imagery used for field mapping of Kausaltar fractures at maps.google.com (last accessed May 2015). Personal communications with Roger Bilham at the Tibet Guest house on 18 May 2015 provided the information about timing of Kausaltar fractures. Earthquake locations and magnitudes shown in Figure 1 were acquired from the National Seismologic Centre, Lainchaur, Kathmandu, Nepal at http://www.seismonepal.gov.np (last accessed July 2015).

ACKNOWLEDGMENTS

Thanks go to the University of Nevada, Reno (UNR) Mackay Earth Sciences and Engineering Department and Graham Kent for funding Pierce and Angster to travel to the epicentral area. The research was supported in part by National Science Foundation (NSF) Grant EAR-1345036. Original Advanced Land Observation Satellite 2 (ALOS-2) data is copyrighted (©2015) by Japanese Aerospace Exploration Agency (JAXA) and was provided under JAXA RA4 project P1372. Part of this research was supported by the National Aeronautics and Space Administration (NASA) Earth Surface and Interior focus area and performed at the Jet Propulsion Laboratory, California Institute of Technology, Pasadena, California. We thank Cunren Liang for processing the ALOS-2 wide-swath interferogram and Susan Owen of the Advanced Rapid Imaging and Analysis (ARIA) project for processing the Global Positioning System (GPS) offsets. Raw GPS data were provided by Jean-Phillipe Avouac with the help of UNAVCO and the Nepal Department of Mines and Geology. We also thank Susan Hough, Roger Bilham, and an anonymous reviewer for reviews and comments that were critical for preparing this manuscript.

For this study, E. F. performed Interferometric Synthetic Aperture Radar (InSAR) analysis and provided guidance on interpretation, T. N. and Y. K. provided fault and lineament maps for guidance in the field, and B. U., D. C., S. A., I. P., and S. W. conducted the field reconnaissance. This work is Center of Neotectonics Contribution Number 65.

REFERENCES

Asahi, K. (2003). Thankot active fault in the Kathmandu Valley, Nepal Himalaya, *J. Nepal Geol. Soc.* **28,** 1–8.

Berberian, M. (1995). Master blind thrust faults hidden under the Zagros folds—Active basement tectonics and surface morphotectonics, *Tectonophysics* **241,** nos. 3/4, 193–224.

Bollinger, L., S. N. Sapkota, P. Tapponnier, Y. Klinger, M. Rizza, J. Van der Woerd, D. R. Tiwari, R. Pandey, A. Bitri, and S. B. de Berc (2014). Estimating the return times of great Himalayan earthquakes in eastern Nepal: Evidence from the Patu and Bardibas strands of the Main Frontal thrust, *J. Geophys. Res.* **119,** no. 9, 7123–7163.

Bonapace, C., and V. Sestini (2003). *Traditional Materials and Construction Technologies Used in the Kathmandu Valley*, Paragraphic for the United Nations Educational, Scientific, and Cultural Organization, Paris, France, 1–165.

Fielding, E. J., C. Liang, S. Samsonov, P. Agram, M.-H. Huang, and S. Sangha (in preparation). Three-dimensional surface deformation from the **M** 7.8 Gorkha earthquake and **M** 7.3 aftershock in Nepal measured by SAR interferometry and pixel offsets (in preparation).

Hinzen, K.-G. (2009). Sensitivity of earthquake-toppled columns to small changes in ground motion and geometry, *Israel J. Earth Sci.* **58,** 309–326.

Lave, J., D. Yule, S. N. Sapkota, K. Basant, C. Madden, M. Attal, and R. Pandey (2005). Evidence for a great medieval earthquake (~1100 A. D.) in the Central Himalayas, Nepal, *Science* **307,** 1302–1305.

Lindsey, E., R. Natsuaki, X. Xu, M. Shimada, H. Hashimoto, D. Melgar, and D. Sandwell (2015). Line of sight deformation from ALOS-2 interferometry: M_w 7.8 Gorka earthquake and 7.3 aftershock, *Geophys. Res. Lett.* **42,** doi: 10.1002/2015GL065385.

Martin, S. S., S. E. Hough, R. Bilham, and C. Hung (2015). Ground motions from the 2015 **M** 7.8 Gorkha, Nepal earthquake constrained by a detailed assessment of macroseismic data, *Seismol. Res. Lett.* **86,** no. 6, doi: 10.1785/0220150138.

Nakata, T. (1989). Active faults of the Himalaya of India and Nepal, *Geol. Soc. Am. Spec. Pap.* **232,** 243–264.

Nakata, T., S. Iwata, H. Yamanaka, H. Yagi, and H. Maemoku (1984). Tectonic landforms of several active faults in the western Nepal Himalayas, *J. Nepal Geol. Soc.* **4,** 177–200.

Noh, M., I. Howat, C. Porter, P. Morin, M. Clementz, and M. Cloutier (2015). *Kathmandu Area Pre-Event DEM Mosaic 8m*, Vol. 2015, Polar Geospatial Center, http://www.pgc.umn.edu/elevation (last accessed May 2015).

Pallares, F. J., A. Aguero, and M. Martin (2006). Seismic behaviour of industrial masonry chimneys, *Int. J. Solid. Struct.* **43,** nos. 7/8, 2076–2090.

Pallares, F. J., S. Ivorra, L. Pallares, and J. M. Adam (2011). State of the art of industrial masonry chimneys: A review from construction to strengthening, *Constr. Build. Mater.* **25,** 4351–4361.

Paudyal, Y. R., R. Yatabe, N. P. Bhandary, and R. K. Dahal (2012). Basement topography of the Kathmandu basin using microtremor observations, *J. Asian Earth Sci.* **62,** 627–637.

Rosen, P. A., E. Gurrola, G. F. Sacco, and H. Zebker (2012). The InSAR Scientific Computing Environment, *Proceedings of the 9th European Conference on Synthetic Aperture Radar*, Nuremberg, Germany, 23–26 April 2012, 730–733.

Sapkota, S. N., L. Bollinger, Y. Klinger, P. Tapponnier, Y. Gaudemer, and D. Tiwari (2013). Primary surface ruptures of the great Himalayan earthquakes in 1934 and 1255, *Nat. Geosci.* **6,** no. 1, 71–76.

Wesnousky, S. G. (2008). Displacement and geometrical characteristics of earthquake surface ruptures: Issues and implications for seismic-hazard analysis and the process of earthquake rupture, *Bull. Seismol. Soc. Am.* **98,** no. 4, 1609–1632.

Yeats, R. S., and R. J. Lillie (1991). Contemporary tectonics of the Himalayan frontal fault system—Folds, blind thrusts and the 1905 Kangra earthquake, *J. Struct. Geol.* **13,** no. 2, 215–225.

Stephen Angster
Steven Wesnousky
Ian Pierce
University of Nevada, Reno
Center for Neotectonics Studies
MS169, 1664 North Virginia Street
Reno, Nevada 89557 U.S.A.
sangster@nevada.unr.edu

Eric J. Fielding
Jet Propulsion Laboratory
California Institute of Technology
MS 300-233 4800 Oak Grove Drive
Pasadena, California U.S.A.

Deepak Chamlagain
Department of Geology
Tri-Chandra Multiple Campus
Tribhuvan University
TU Road
Kirtipur 44618, Kathmandu, Nepal

Dipendra Gautam
Center for Disaster and Climate Change Studies
GPO Box 21560
Kathmandu, Nepal

Bishal Nath Upreti
Nepal Academy of Science and Technology (NAST)
GPO Box 3323
Khumaltar, Lalitpur, Nepal

Yasuhiro Kumahara
Graduate School of Education
Hiroshima University
1-1-1 Kagamiyama
Higashihiroshima, 739-8524, Japan

Takashi Nakata
Department of Geography
Hiroshima University
1-3-1 Kagamiyama
Higashihiroshima, 739-8526, Japan